High thermoelectricpower factor in graphene/hBN devices

Junxi Duan[a,b,c], Xiaoming Wang[b], Xinyuan Lai[a], Guohong Li[a], Kenji Watanabe (渡邊賢司)[d], Takashi Taniguchi[d], Mona Zebarjadi[b,c,1], and Eva Y. Andrei[a,c,1]

[a]Department of Physics and Astronomy, Rutgers University, Piscataway, NJ 08854; [b]Department of Mechanical and Aerospace Engineering, Rutgers University, Piscataway, NJ 08854; [c]Institute of Advanced Materials, Devices, and Nanotechnology, Rutgers University, Piscataway, NJ 08854; and [d]Advanced Materials Laboratory, National Institute for Materials Science, 1-1 Namiki, Tsukuba 305-0044, Japan

Contributed by Eva Y. Andrei, October 26, 2016 (sent for review July 26, 2016; reviewed by Shuo Chen, Steve Cronin, and Mildred S. Dresselhaus)

Fast and controllable cooling at nanoscales requires a combination of highly efficient passive cooling and active cooling. Although passive cooling in graphene-based devices is quite effective due to graphene's extraordinary heat conduction, active cooling has not been considered feasible due to graphene's low thermoelectric power factor. Here, we show that the thermoelectric performance of graphene can be significantly improved by using hexagonal boron nitride (hBN) substrates instead of SiO_2. We find the room temperature efficiency of active cooling in the device, as gauged by the power factor times temperature, reaches values as high as 10.35 $W{\cdot}m^{-1}{\cdot}K^{-1}$, corresponding to more than doubling the highest reported room temperature bulk power factors, 5 $W{\cdot}m^{-1}{\cdot}K^{-1}$, in $YbAl_3$, and quadrupling the best 2D power factor, 2.5 $W{\cdot}m^{-1}{\cdot}K^{-1}$, in MoS_2. We further show that the Seebeck coefficient provides a direct measure of substrate-induced random potential fluctuations and that their significant reduction for hBN substrates enables fast gate-controlled switching of the Seebeck coefficient polarity for applications in integrated active cooling devices.

graphene | Seebeck coefficient | thermoelectric power factor | electron–hole puddles | screened Coulomb scattering

As the size of the electronic components shrinks, larger power densities are generated, resulting in local hot spots. The small size of these hot spots and their inaccessibility make it difficult to maintain a low and safe operating temperature (1). Solid-state integrated active thermoelectric coolers could solve the long-lasting electronic cooling problem (2, 3). These coolers are designed to actively pump heat in its natural flow direction, from the hot spots generated on the chip to the colder ambient reservoir. In this mode of operation, active cooling assists passive cooling, which is different from the refrigeration mode where passive and active cooling oppose each other (4). In passive cooling, heat is transported via the phonon channel, and the heat flux is set by the thermal conductance of the cooler. In contrast, active cooling uses the Peltier cooling to pump heat via the electronic channel and can be controlled and tuned with applied current. The performance of Peltier cooling is a function of the thermoelectric power factor, $PF=\sigma S^2$, where σ is the electrical conductivity and S is the Seebeck coefficient. In this manuscript, we also use the notation of PFT, referring to PF times temperature T, which has a more convenient unit of watts per meter kelvin, the same as thermal conductivity. Unlike common thermoelectric applications, where the ability of a material to efficiently produce thermoelectric power is measured by its dimensionless figure of merit, $ZT=\sigma S^2 T/\kappa$ (κ is the thermal conductivity), thermoelectric cooling does not require low thermal conductivity. In fact, both the power factor and the thermal conductivity should be large. Although there is no theoretical limit on PF, the interplay between the Seebeck coefficient and the electrical conductivity in highly doped bulk semiconductors, has so far prevented the realization of very large thermoelectric power factors (5–7).

Single-layer graphene possesses extraordinary electronic and thermal properties (8–12). In particular, its high mobility, which due to the weak electron–phonon interaction persists up to room temperature, can be orders of magnitude higher than in other 2D thermoelectric materials, such as semiconducting transition metal dichalcogenides (13–16). Theoretical and experimental studies show that the Seebeck coefficient in graphene could reach values comparable to that in bulk semiconductors by decreasing the carrier density (17–23). The combination of graphene's large mobility and competitive Seebeck coefficient result in large power factor and large active cooling. At the same time, graphene's extremely large thermal conductivity also enables efficient passive cooling (12). Furthermore, the ability to control its carrier density by electrostatic gating rather than by chemical doping imparts to graphene an important advantage over bulk materials. Note that graphene owns low ZT because of its large thermal conductivity, and therefore it is only suitable for applications such as electronic cooling, which is the focus of this work.

As a purely 2D material, the electronic properties of graphene are strongly affected by its surroundings. Experiments demonstrate that the commonly used SiO_2 substrate has surface charge states and impurities that cause Coulomb scattering that limits the mobility and introduce large potential fluctuations in G/SiO_2 samples (24–26). The potential fluctuations induce electron–hole puddles (EHPs) in the vicinity of the charge-neutrality

Significance

The miniaturization of electronic components and the excessive heating produced by the increased power densities in these small devices has heightened the need for on-chip cooling solutions. This has prompted a search for materials with large thermoelectric power factor and thermal conductivity that could be integrated in active thermoelectric coolers. Here, we report record thermoelectric power factors achieved in graphene on hexagonal boron nitride devices, corresponding to more than doubling the highest reported room temperature bulk values. In these devices, the smooth and highly efficient gating between electron- and hole-doped sectors, which facilitates switching the polarity of the Seebeck coefficient, extends a distinct advantage for on-chip thermoelectric cooling applications. Based on these results, we propose an integrated graphene-based active on-chip cooler.

Author contributions: J.D., M.Z., and E.Y.A. designed research; J.D. and X.L. performed research; G.L. provided valuable advice about measurement and analysis; J.D., K.W., and T.T. contributed new reagents/analytic tools; J.D., X.W., M.Z., and E.Y.A. analyzed data; and J.D., M.Z., and E.Y.A. wrote the paper.

Reviewers: S. Chen, University of Houston; S. Cronin, University of Southern California; and M.S.D., Massachusetts Institute of Technology.

The authors declare no conflict of interest.

[1]To whom correspondence may be addressed. Email: eandrei@physics.rutgers.edu or m.zebarjadi@virginia.edu.

This article contains supporting information online at www.pnas.org/lookup/suppl/doi:10.1073/pnas.1615913113/-/DCSupplemental.

point (CNP) and prevent gating for lower carrier density (25). Depositing graphene on hexagonal boron nitride (hBN) substrates (G/hBN), which are relatively inert and free of surface charge traps, produces samples with smaller potential fluctuations and higher mobility than G/SiO_2 (27–29). Here, we report on comparable measurements of the thermoelectric properties for G/hBN and G/SiO_2 samples.

Fig. 1*A* shows a schematic of the apparatus for measuring the electrical and thermal transport properties (*Supporting Information*). Fig. 1*B* shows the gate voltage (V_g) dependence of the Seebeck coefficient, $S(V_g)$, measured in G/hBN and G/SiO_2 devices at 290 K. In both devices, $S(V_g)$ is positive (negative) in the hole (electron)-doped sector. Its absolute value increases with decreased doping, reaches a peak value S_p at gate voltage V_p before vanishing at the CNP. We note that, in the G/hBN device, S_p = 182 μV/K and V_p = −2.2 V define a much sharper peak than in the G/SiO_2 device, where S_p = 109 μV/K and V_p = −4.5 V. From the measured values of S and the conductivity of the devices, we calculate the value of $PFT = S^2\sigma T$ as a function of carrier density shown in Fig. 1*C* (30). The *PFT* first increases with decreasing carrier density when far from CNP, and then after reaching a peak value, it drops rapidly to zero at the CNP. We find that the room temperature peak value of *PFT* in the G/hBN device, 10.35 $W \cdot m^{-1} \cdot K^{-1}$, is almost twice that in the G/SiO_2 device, 6.16 $W \cdot m^{-1} \cdot K^{-1}$. This value is larger than the record value in bulk materials at room temperature reported for $YbAl_3$ (∼5 $W \cdot m^{-1} \cdot K^{-1}$), and larger than the value at room temperature in 2D materials reported for MoS_2 (∼2.5 $W \cdot m^{-1} \cdot K^{-1}$) and WSe_2 (∼1.2 $W \cdot m^{-1} \cdot K^{-1}$) (30–33). As we discuss later, the *PFT* value increases with temperature, and because it is not yet saturated at room temperature, even larger *PFT* values are expected at higher temperatures.

We next use the linear Boltzmann equation in the relaxation time approximation to relate the Seebeck coefficient to the experimentally controlled quantities. Within this model, the response of the electrical and thermal current densities, j and j_q, to the electric field, E, and temperature gradient, ∇T, are given by the following (17):

$$j = L^{11}E + L^{12}(-\nabla T), \quad [1]$$

$$j_q = L^{21}E + L^{22}(-\nabla T), \quad [2]$$

where $L^{11} = K^{(0)}$, $L^{12} = -(1/eT)K^{(1)}$, $L^{21} = -(1/e)K^{(1)}$, $L^{22} = K^{(2)}/e^2T$, and

$$K^{(m)} = \int_{-\infty}^{+\infty} d\epsilon(\epsilon-\mu)^m\left(-\frac{\partial f^0(\epsilon)}{\partial\epsilon}\right)\sigma(\epsilon) \quad m = 0,1,2. \quad [3]$$

Here, $\epsilon(k) = \hbar v_F k$, v_F is the Fermi velocity, μ is the chemical potential, $f^0(\epsilon) = 1/(1+\exp((\epsilon-\mu)/k_BT))$ is the equilibrium Fermi–Dirac distribution function, and k_B is the Boltzmann constant. The differential conductivity is $\sigma(\epsilon) = e^2v_F^2(D(\epsilon)\tau(\epsilon)/2)$, where $D(\epsilon) = 2|\epsilon|/(\pi\hbar^2v_F^2)$ is the density of states including the fourfold degeneracy of graphene, $v_F = 10^6$ $m \cdot s^{-1}$ is the Fermi velocity (34), and $\tau(\epsilon)$ is the relaxation time. The Seebeck coefficient is defined as $S = L^{12}/L^{11}$, the electrical and thermal conductivity are $\sigma = L^{11}$ and $\kappa = L^{22}$, respectively, and the Peltier coefficient is $\Pi = L^{21}/L^{11}$ (17, 35). Importantly, we note that the Seebeck coefficient is controlled by the energy dependence of the conductivity.

In Fig. 1*D*, we show the calculated carrier density dependence of the Seebeck coefficient at 300 K in the presence of random potential fluctuations (RPFs) induced by charge impurities (*Supporting Information*). The calculation follows the model proposed in ref. 17 and, for simplicity, considers only the screened Coulomb scattering, which is known to be dominant in this system at low carrier densities (15, 17, 36–38). We note that

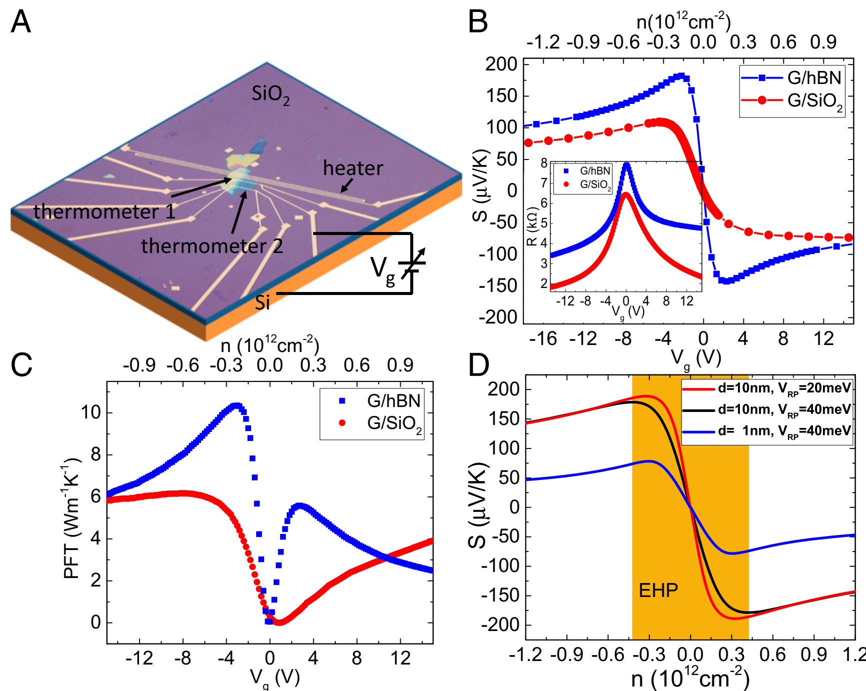

Fig. 1. Thermoelectric measurement of graphene at room temperature. (*A*) Optical micrograph of the graphene on hBN (G/hBN) device. (*B*) Measured Seebeck coefficient in G/hBN and G/SiO_2 devices as a function of back gate at 290 K. (*Inset*) Measured resistance vs. V_g in both devices at 290 K. (*C*) Measured *PFT* in both samples as a function of back gate at 290 K. (*D*) Simulation of carrier density dependence of the Seebeck coefficient at 300 K using the screened Coulomb-scattering model for two values of the hBN thickness, d, and random potential fluctuations, V_{RP}, induced by charge impurities (*Supporting Information*). The rectangular shadow corresponds to the EHP region in a sample with d = 10 nm and V_{RP} = 40 meV.

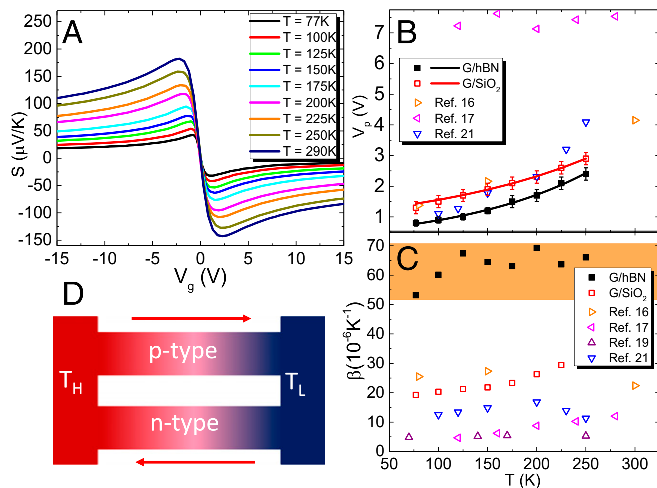

Fig. 2. Temperature dependence of the Seebeck coefficient and EHP region. (*A*) Measured Seebeck coefficient in the G/hBN device as a function of backgate voltage and temperature. (*B*) Temperature dependence of peak positions of the Seebeck coefficient (V_p) on the hole side for G/hBN (solid squares) and G/SiO_2 (open squares) devices are shown together with the exponential fit discussed in the text (solid lines). (*C*) Slope of polarity-switching effect, β, for both devices (solid squares for G/hBN and open squares for G/SiO_2). Values of V_p and β in G/SiO_2 samples (open triangles) extracted from previous studies are also shown. (*D*) Sketch of the proposed graphene-based active cooling device with integrated n-type and p-type legs.

the monotonic increase of S with decreasing carrier density peaks at the point where the Fermi energy enters the EHP region (17, 18). In this region (shadow area in Fig. 1*D*), both electrons and holes are present, but because they contribute oppositely to S, the value of S drops. Consequently, the narrower the energy range of the EHP region, the higher the peak value of S. There is, however, a limit to the magnitude of S that is set by the temperature. When k_BT becomes comparable to the energy scale of the RPF, the temperature starts controlling the value of S_p. The effect of inserting the hBN spacer, typically $d \sim 10$ nm, is to increase the distance from the charge impurities in the SiO_2 substrate, which not only reduces the magnitude of the RPF in the graphene plane but also increases the electron–hole asymmetry resulting in a larger value of S_p (*Supporting Information*). Again, there is a limit to this improvement. For infinitely large separation, that is, no Coulomb scattering, thermally excited phonons become the dominant mechanism that limits the value of S. In the acoustic phonon-dominated regime, the Seebeck coefficient at room temperature is expected to be smaller than S = 100 μV/K (17).

As discussed above, V_p marks the boundary of the EHP region, which depends on both the temperature and the extent of the RPF. In the high-temperature limit, this region is dominated by thermal excitations, whereas at low temperatures it is controlled by the energy scale of the RPF. Currently, most measurements of the EHP are carried out by scanning probe microscopy, which are typically performed at low temperatures and over a scanning range much smaller than the size of transport devices (28, 29, 39). Although the boundary of the EHP region can be estimated from the gate dependence of the resistivity (27), V_p provides a more direct measure of the EHP region. In Fig. 2*A*, showing the back-gate dependence of S in the temperature range of 77–290 K, we note that as the temperature decreases S_p moves closer to the CNP while at the same time its magnitude diminishes.

In the following discussion, we focus on the hole side because the peaks on this side are clearer in the G/SiO_2 sample. The temperature dependence of V_p, shown in Fig. 2*B* for both samples, follows an exponential function, $V_p(T) = a + b(e^{\alpha T} - 1)$, where a, b, and α are fitting parameters. The intercept a at T = 0 provides access to the carrier density fluctuations (EHP region) and to the magnitude of the RPF. From the data in Fig. 2*B*, we find a = 0.12 and 0.52 V for the G/hBN and G/SiO_2 samples, respectively. This corresponds to carrier density fluctuations of 1.8×10^{10} and 7.6×10^{10} cm^{-2}, and to RPF energy scales of 21.8 and 45.4 meV for the G/hBN and G/SiO_2 samples, respectively. Both values are comparable to previous results measured by scanning tunneling microscopy at liquid-helium temperature (29). A comparison with the temperature dependence of V_p extracted from previous studies shows that the hBN substrates produce significantly narrower peaks in $S(V_g)$ corresponding to the superior sample quality with a substantial reduction in the range of the RPF.

Unlike the case of the voltage drop in electrical transport measurements, which is insensitive to the sign of the carrier charge, the Seebeck voltage reverses its sign when switching from hole doping to electron doping. In the G/hBN sample, the polarity of S_p can be reversed with a relatively small gate voltage ~$2V_P$. We define β as the slope of the polarity-switching effect: $\beta = S_p/V_p$. A comparison of β values in G/hBN and in G/SiO_2 samples in both the present and earlier studies clearly shows that the switching efficiency is substantially enhanced in G/hBN (Fig. 2*C*).

The bipolar nature of graphene, which allows smooth gating between electron- and hole-doped sectors, together with the large values of β, which facilitate switching the polarity of S, extend a distinct advantage for on-chip thermoelectric cooling applications. This can be seen in the thermoelectric active cooler design shown in Fig. 2*D*, which can pump heat from the hot end (T_H) to the cold end (T_L) in a controlled and fast manner using combined active and passive cooling effects. In this G/hBN-based device, the p–n legs are arranged thermally in parallel and electrically in series to maximize the active cooling (4). Its structure is readily realized with lithographically patterned gates because gating is more effective in 2D devices than in bulk devices where charge carriers will accumulate near the interface. Also, unlike the doping method, gating will not introduce extra charge-scattering centers. At the optimal value of the applied current, the active cooling power of the device is $P_{active} = PFT_H \cdot T_H/2$ (4). On the other hand, the passive cooling power is $P_{passive} = \kappa \Delta T$, where $\kappa \sim 600$ $W{\cdot}m^{-1}{\cdot}K^{-1}$ is the thermal conductivity of graphene supported on a substrate at room temperature (12). For $T_H = 330$ K and $\Delta T = 30$ K, active cooling contributes an additional 10% over the passive cooling. At higher temperatures, as *PFT* increases and the thermal conductivity decreases, the contribution of active cooling further increases.

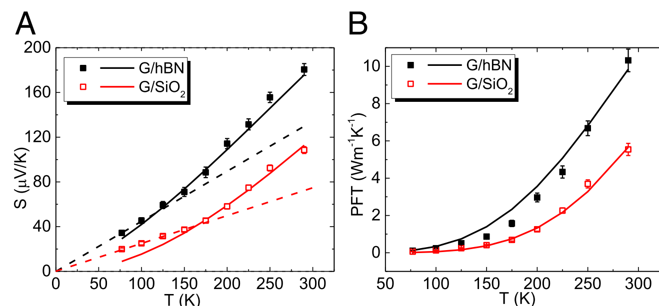

Fig. 3. Temperature dependence of the Seebeck coefficient and *PFT* at fixed carrier density. (*A*) Measured Seebeck coefficient in G/hBN ($n = -0.2 \times 10^{12}$ cm^{-2}, solid squares) and G/SiO_2 ($n = -0.3 \times 10^{12}$ cm^{-2}, open squares) devices are plotted together with the theoretical values (solid lines) calculated by using the screened Coulomb-scattering model discussed in the text. Dashed lines serve as guides to emphasize the nonlinear behavior. (*B*) Measured *PFT* (same density as in *A*; solid and open squares) from both devices are compared with theoretical values (solid lines).

The temperature dependence $S(T)$ at a fixed back-gate voltage for both samples is shown in Fig. 3*A*. The corresponding carrier density in G/hBN and G/SiO_2 is -0.2×10^{12} and -0.3×10^{12} cm^{-2}, respectively. We note that, for both devices studied here, $S(T)$ does not follow the linear dependence (dashed lines) expected from Mott's equation (40). To understand this result, we must take into account the screened Coulomb scattering, which plays an important role in both samples. In the G/SiO_2 sample, screened Coulomb scattering is the dominant mechanism as indicated by the linear dependence of the conductivity on carrier density (27, 41, 42). In the G/hBN samples, Coulomb scattering is also dominant at low carrier density, but at higher densities it crosses over to short-range impurity scattering (*Supporting Information*) (27). Therefore, to present a meaningful comparison between the two samples, we choose a carrier density smaller than the crossover point for the G/hBN sample. Using the screened Coulomb scattering model in the linear response theory to calculate $S(T)$ and with only one fitting parameter (*Supporting Information*), we obtain the solid lines in Fig. 3*A*, which show good agreement with the measured quadratic T dependence of the $S(T)$ curves (17). Similarly, the temperature dependence of the measured and calculated *PFT* are shown in Fig. 3*B*. In the calculation, inelastic electron–phonon interaction is not included because the screened Coulomb scattering is dominant in this temperature range as indicated by the energy scale of the RPF. However, electron–phonon scattering could become important when the temperature yields a k_BT that is much higher than the energy of RPF as in the case for hBN-encapsulated graphene devices (43).

In summary, we have shown that S_p in G/hBN device reaches twice the value measured in G/SiO_2 device and its peak *PFT* value of 10.35 $W \cdot m^{-1} \cdot K^{-1}$ significantly exceeds previously reported records in both 2D and 3D thermoelectric materials. We demonstrate that the peak of the $S(V_g)$ curves provides a direct measure of the RPF and substrate quality through the width of the EHP region. In particular, we find a fourfold reduction of the RPF in G/hBN, compared with G/SiO_2 samples. We further show that the bipolar switching slope is significantly larger in the G/hBN devices, which makes it possible to integrate all-in-one graphene p-type and n-type devices. The study demonstrates the advantage of using graphene in thermoelectric applications especially in electronic cooling where large thermal conductivity (passive cooling) and large thermoelectric power factor (active cooling) are needed simultaneously.

Methods

Graphene on hBN samples are fabricated using the poly(methyl methacrylate) (PMMA)-based dry transfer method (44). hBN is exfoliated on a 300-nm SiO_2/Si substrate. The hBN thickness is measured by atomic-force microscopy (AFM). Single-layer graphene is prepared on a PMMA membrane. It could be identified by optical microscopy through the color contrast and after the transfer by AFM and Raman measurements. In the case of G/SiO_2, the graphene flake is directly exfoliated on the SiO_2 surface. Electrodes on the graphene sample serve as voltage probes and thermometers measuring the local temperature at the two ends of graphene flake. A strip of gold wire next to the sample is used as a heater. Fig. 1*A* shows the optical micrograph of a typical sample. To induce a uniform temperature gradient across the sample, the size of the heater (400 μm) is much larger than the size of the graphene flake (typically 20 μm × 10 μm) and thermometers (40 μm). Thermometers and heater are defined by standard electron beam lithography. Cr/Au (3/45-nm) layers are deposited using electron beam evaporation. All of the samples are annealed in forming gas (H_2/Ar) at 230 °C over 12 h to remove resist residue before measurements.

The temperature is measured through the four-probe resistance of the thermometers with resolution smaller than 0.01 K. By powering up the heater, a temperature gradient ΔT is generated along the sample (Fig. 1*A*). The thermally induced voltage ΔV is measured by the voltage probes at the two ends of the sample. The Seebeck coefficient is then calculated using the following: $S = -\Delta V/\Delta T$. $\Delta T \ll T$ is required to make the measurement in the linear response regime. All of the measurements are carried out in vacuum ($P \sim 10^{-6}$ Pa) over a temperature range of 77–300 K.

Associated Content. *Supporting Information* includes the following: device characterization, Seebeck measurement, summary of recently reported *PFT* in 2D materials, nonlinear dependence on temperature, results from other G/hBN samples, thermal conductivity and thermoelectric figure of merit, and calculation details.

ACKNOWLEDGMENTS. M.Z. and J.D. acknowledge support from the Air Force Young Investigator Award (Grant FA9550-14-1-0316), E.Y.A. acknowledges support from Grant DOE-FG02-99ER45742, and J.D. acknowledges support from National Science Foundation Grant DMR 1207108.

1. Pop E, Sinha S, Goodson KE (2006) Heat generation and transport in nanometer-scale transistors. *Proc IEEE* 94(8):1587–1601.
2. Snyder GJ, Toberer ES (2008) Complex thermoelectric materials. *Nat Mater* 7(2):105–114.
3. Vaqueiro P, Powell AV (2010) Recent developments in nanostructured materials for high-performance thermoelectrics. *J Mater Chem* 20(43):9577–9584.
4. Zebarjadi M (2015) Electronic cooling using thermoelectric devices. *Appl Phys Lett* 106(20):203506.
5. Zebarjadi M, et al. (2011) Power factor enhancement by modulation doping in bulk nanocomposites. *Nano Lett* 11(6):2225–2230.
6. Zebarjadi M, Liao B, Esfarjani K, Dresselhaus M, Chen G (2013) Enhancing the thermoelectric power factor by using invisible dopants. *Adv Mater* 25(11):1577–1582.
7. Liang W, et al. (2009) Field-effect modulation of Seebeck coefficient in single PbSe nanowires. *Nano Lett* 9(4):1689–1693.
8. Geim AK, Novoselov KS (2007) The rise of graphene. *Nat Mater* 6(3):183–191.
9. Novoselov KSA, et al. (2005) Two-dimensional gas of massless Dirac fermions in graphene. *Nature* 438(7065):197–200.
10. Zhang Y, Tan YW, Stormer HL, Kim P (2005) Experimental observation of the quantum Hall effect and Berry's phase in graphene. *Nature* 438(7065):201–204.
11. Balandin AA, et al. (2008) Superior thermal conductivity of single-layer graphene. *Nano Lett* 8(3):902–907.
12. Seol JH, et al. (2010) Two-dimensional phonon transport in supported graphene. *Science* 328(5975):213–216.
13. Bolotin KI, Sikes KJ, Hone J, Stormer HL, Kim P (2008) Temperature-dependent transport in suspended graphene. *Phys Rev Lett* 101(9):096802.
14. Chen JH, Jang C, Xiao S, Ishigami M, Fuhrer MS (2008) Intrinsic and extrinsic performance limits of graphene devices on SiO_2. *Nat Nanotechnol* 3(4):206–209.
15. Hwang EH, Das Sarma S (2009) Screening-induced temperature-dependent transport in two-dimensional graphene. *Phys Rev B* 79(16):165404.
16. Radisavljevic B, Radenovic A, Brivio J, Giacometti V, Kis A (2011) Single-layer MoS_2 transistors. *Nat Nanotechnol* 6(3):147–150.
17. Hwang EH, Rossi E, Das Sarma S (2009) Theory of thermopower in two-dimensional graphene. *Phys Rev B* 80(23):235415.
18. Zuev YM, Chang W, Kim P (2009) Thermoelectric and magnetothermoelectric transport measurements of graphene. *Phys Rev Lett* 102(9):096807.
19. Checkelsky JG, Ong NP (2009) Thermopower and Nernst effect in graphene in a magnetic field. *Phys Rev B* 80(8):081413.
20. Wei P, Bao W, Pu Y, Lau CN, Shi J (2009) Anomalous thermoelectric transport of Dirac particles in graphene. *Phys Rev Lett* 102(16):166808.
21. Nam SG, Ki DK, Lee HJ (2010) Thermoelectric transport of massive Dirac fermions in bilayer graphene. *Phys Rev B* 82(24):245416.
22. Wang CR, et al. (2011) Enhanced thermoelectric power in dual-gated bilayer graphene. *Phys Rev Lett* 107(18):186602.
23. Wang DQ, Shi J (2011) Effect of charged impurities on the thermoelectric power of graphene near the Dirac point. *Phys Rev B* 83(11):113403.
24. Ishigami M, Chen JH, Cullen WG, Fuhrer MS, Williams ED (2007) Atomic structure of graphene on SiO_2. *Nano Lett* 7(6):1643–1648.
25. Martin J, et al. (2008) Observation of electron-hole puddles in graphene using a scanning single-electron transistor. *Nat Phys* 4(2):144–148.
26. Andrei EY, Li G, Du X (2012) Electronic properties of graphene: A perspective from scanning tunneling microscopy and magnetotransport. *Rep Prog Phys* 75(5):056501.
27. Dean CR, et al. (2010) Boron nitride substrates for high-quality graphene electronics. *Nat Nanotechnol* 5(10):722–726.
28. Xue J, et al. (2011) Scanning tunnelling microscopy and spectroscopy of ultra-flat graphene on hexagonal boron nitride. *Nat Mater* 10(4):282–285.
29. Decker R, et al. (2011) Local electronic properties of graphene on a BN substrate via scanning tunneling microscopy. *Nano Lett* 11(6):2291–2295.
30. Dehkordi AM, Zebarjadi M, He J, Tritt TM (2015) Thermoelectric power factor: Enhancement mechanisms and strategies for higher performance thermoelectric materials. *Mater Sci Eng Rep* 97:1–22.
31. Hippalgaonkar K, et al. (2015) Record high thermoelectric power factor in single and few-layer MoS_2. arXiv:1505.06779.
32. Kayyalha M, Shi L, Chen YP (2015) Gate-tunable and thickness-dependent electronic and thermoelectric transport in few-layer MoS_2. arXiv:1505.05891.
33. Yoshida M, et al. (2016) Gate-optimized thermoelectric power factor in ultrathin WSe_2 single crystals. *Nano Lett* 16(3):2061–2065.

34. Luican A, et al. (2011) Single-layer behavior and its breakdown in twisted graphene layers. *Phys Rev Lett* 106(12):126802.
35. Esfarjani K, Zebarjadi M, Kawazoe Y (2006) Thermoelectric properties of a nanocontact made of two-capped single-wall carbon nanotubes calculated within the tight-binding approximation. *Phys Rev B* 73(8):085406.
36. Hwang EH, Adam S, Sarma SD (2007) Carrier transport in two-dimensional graphene layers. *Phys Rev Lett* 98(18):186806.
37. Adam S, Hwang EH, Galitski VM, Das Sarma S (2007) A self-consistent theory for graphene transport. *Proc Natl Acad Sci USA* 104(47):18392–18397.
38. Tan YW, et al. (2007) Measurement of scattering rate and minimum conductivity in graphene. *Phys Rev Lett* 99(24):246803.
39. Lu CP, et al. (2016) Local, global, and nonlinear screening in twisted double-layer graphene. *Proc Natl Acad Sci USA* 113(24):6623–6628.
40. Cutler M, Mott NF (1969) Observation of Anderson localization in an electron gas. *Phys Rev* 181(3):1336.
41. Chen JH, et al. (2008) Charged-impurity scattering in graphene. *Nat Phys* 4(5): 377–381.
42. Hong X, Zou K, Zhu J (2009) Quantum scattering time and its implications on scattering sources in graphene. *Phys Rev B* 80(24):241415.
43. Ghahari F, et al. (2016) Enhanced thermoelectric power in graphene: Violation of the Mott relation by inelastic scattering. *Phys Rev Lett* 116(13):136802.
44. Mao J, et al. (2016) Realization of a tunable artificial atom at a supercritically charged vacancy in graphene. *Nat Phys* 12(6):545–549.
45. Gorbachev RV, et al. (2011) Hunting for monolayer boron nitride: Optical and Raman signatures. *Small* 7(4):465–468.
46. Xu X, et al. (2014) Length-dependent thermal conductivity in suspended single-layer graphene. *Nat Commun* 5:3689.
47. Balandin AA (2011) Thermal properties of graphene and nanostructured carbon materials. *Nat Mater* 10(8):569–581.
48. Saito K, Nakamura J, Natori A (2007) Ballistic thermal conductance of a graphene sheet. *Phys Rev B* 76(11):115409.
49. Yigen S, Tayari V, Island JO, Porter JM, Champagne AR (2013) Electronic thermal conductivity measurements in intrinsic graphene. *Phys Rev B* 87(24):241411.